4.3   State of the art

The shift of the brain during the operation represents a major source of inaccuracy for any system employing pre-operative images. Because the actual position of the brain during the operation differs from the estimation provided by previous images, the information available to neuronavigators will present systematically misregistrations, and thus surgeons will have to deal manually with possible inconsistencies.

A number of papers quantifying the magnitude and direction of the shift exists. A simple approach is to monitor the locations of a number of landmarks in the exposed surface of the brain through the operation. Roberts [82] employs for this purpose an operating microscope on a ceiling-mounted robotic platform with tracking capabilities. The statistical analysis of the recorded positions show displacement on the order of 1 cm, mostly along the gravity axis.

Maureer [68] employs an intraoperative MR device to acquire a number of scannings during the intervention. This procedure is applied to different interventions of different type (biopsies, functional and resections), and then images are analysed to search for volume changes, and also registered with a non-rigid algorithm based on mutual information. The results, though preliminary, suggest that little deformations occur to the tentorium and the hemisphere contralateral to the procedure, and that deformations up to 4.5 mm may occur in zones up to 1 cm around the resection. This paper was written during my first stage in CISG, which gave me the chance to provide some small contribution to the research procedures.

Another paper employing a similar procedure with intraoperative MR device is [74]. The authors distinguish two anatomical compartments (surface and subsurface) and measures the diameter of the resection cavity and the cortical opening in order to provide a complete picture of the different cases that may occur. Their results show that brain shift, even at ventricular levels, occurs in the direction of gravity after craniotomy but before tumour resection. After the resection, the weight of the overlaying tissue has been reduced and reversed motion toward the surgical site occurs. Finally, they measure the shift of the entire exposed hemisphere by comparing the surface of the two volume scans.

Other papers aim at the registration of pre-operative to intra-operative images. Warfield [109] achieves this purpose by using as a template segmented pre-operative images. Ferrant [13] tracks key surfaces using an active surface algorithm, and deformation is inferred from the displacements. Surface shift was estimated to be up to 1cm, and subsurface shift up to 6 mm.

Another interesting problem is to model of the brain to achieve a realistic simulation of the deformations. [28, 108] present two physically-based models for this purpose, with interesting results. The later achieves real-time simulations on the operating room.

The most active group in research and applications based on ecographic images is the Department of Engineering in the University of Cambridge, headed by Dr. R. Prager and Dr. A. Gee. They publish a number of reports giving full details of their research. Initial papers [85, 83, 84, 88] provide a general review of ultrasound image features and the characteristics of a system for compounding.

They propose several techniques to improve the quality of the compounded image:

an algorithm to deal with multiple swaps, and also a registration step to adjust the position of each acquired slice to the existing volume image. The objective of the registration step is to correct the inaccurate positioning of the tracking device, which otherwise would blur the features in the compounded image. They propose two automatic error correction techniques: a) edgels detected by the Canny operator are aligned with the RANSAC regression technique, and b) correlation of the gradient magnitude in a multipyramid approach.

They provide significant contributions in the calibration of the ecography [79, 78, 86]. They propose the so-called 'Cambridge phantom', a mechanical device designed to exercise all the degrees of freedom in the scanning. This is an important issue in order to achieve a statistically well-posed dataset for the search of the calibration parameters. The idea is a refinement of the process of taking the floor of the water bath for calibration: for the sake of avoiding miss-leading reflections when the floor is scanned in oblique angles, they constraint mechanically the probe to move only in the areas where a proper image of a thin bar can be read. Also, they design an algorithm for the automatic segmentation of the wall in the images, which permits automatic calibration of the probe. They provide a software package, called Stradx, with all these facilities.

Other contributions of this group are:

- model-based shape reconstruction by means of PCA analysis [95, 96].

- radial basis functions to improve the interpolation in the compounded image [87].

- visualisation of the compounded image superimposed to the corresponding area of a mannequin model [101].

- large organ volume measurement with a sequence of B-scans without actual 3–D compounding [100].

The papers reported in this section do not apply yet the full potential provided by the availability of two sources of information: the pre-operative image, and the video sequence during the operation. The later reflects the changes in real time, while the first is easier to interpret and covers the full organ. Therefore it is natural to fuse the information, which is our aim in this chapter by means of two automatic algorithms, based on creaseness measures and similar to those presented in previous chapters.

4.4   A system for compounding ecographies

In this section we give the details of implementation of our system for free-hand ultra-sounding. Although these systems have been described many times in the literature, the full implementation is actually troublesome when, as it was our case, one lacks experience in the area. Required expertise concerned:

topic	requirements
hardware	image acquisition
hardware	tracker communication
robotics	calibration
statistics	numerical issues
software	Visual C++

Also, we were very much conditioned by the fact that our medical partner was physically distant: the whole system had to be small and light enough to permit its transport to the operation theatre. Moreover, the chances of system testing were rather sparse in time (not on a daily basis, like at CISG).

The research was divided in three periods. The first took place during my stage in London, and I had the great benefit to interact with the colleagues in the group who had experience in related areas. For instance, tracking and video acquisition were already working so, after designing the system as a whole, I could concentrate in calibration and compounding. Unfortunately, when the stage was over I had to restart all the research this time with our own tracker and video grabber.

When the design and implementation was completed, we tried for some time to achieve some results with the collaboration of a local hospital. After a number of trials, we had to give up because of many reason, the main one being that the intraoperative ultrasound device became out of order and no other was available.

Therefore we decided to change the goal of the research; instead of aiming at working real-time in a neurosurgery operation, we would study first the accuracy and feasibility with a phantom. Dr. Hill, from the CISG at UMDS hospital, again offered us his collaboration, so the final part of the experiments were carried out there.

	Type	Tracker	Site
1	Ecography	Optotrack	London
2	Numerical experiments	Minibird	Barcelona
3	Ecography	Minibird	London

4.4.1   Technical considerations

As mentioned earlier, the whole system had to be as much portable as possible. The computer, therefore, had to be a lap-top; we purchased a Pentium II working at 366 MHz. We studied the qualities of several tracking devices, namely accuracy, weight, price and provided software. The optical-based systems, like Optotrack, though much more accurate, would be too heavy to be carried easily, and also their price being too high, the choice was a magnetic-based Minibird tracker. The following table lists the references. The RMS error given is provided by the manufacturer.

	Manufacturer	Website	RMS error
Minibird 800	Ascension Technology, Vermont	[98]	1.8 mm
Optotrack 3020	Northern Digital, Ontario, Canada	[8]	0.1 mm

Optical-based trackers suffer from others shortcomings, too. Although they are very convenient when regarding the accuracy, they can be cumbersome in the operation theatre, because often the surgeon forgets that he or she must hold the probe

facing the cameras of the tracker. Many times, in the busy times of the operation, this premise is not kept and the data becomes of no use.

On the other hand, magnetic trackers are very sensitive to neighbouring metallic objects. If this property is already very distracting for in vitro experiments (two weeks were lost until we discovered a metal bar under the experiments desk), it becomes a nightmare in the real operating environment. For this case, we simply could not do better than keeping the transducer as closed to emitter as possible, in order to minimise interferences.

Grabbing the video frames with the laptop caused also some trouble. There are not many frame grabbers available for them; they work slower than those for a table PC, and they run only under Microsoft Windows. Also, the technical specifications do not report clearly the frames per second it can capture, so comparing them becomes more troublesome. Our choice was the Videoport Framegrabber, Transtech systems, Hants, U.K. See figure in page 163 for an actual picture of the whole system. [97].

When the equipment was complete, we programmed the software to grab the frames and track the position of the transducer in real time. Two choices could be taken: to grab as many frames as possible, and then save them, or rather save individually each one after its acquisition. The first implied a delay of 20 seconds after each acquisition, spent on writing to the hard disk. The second could record without pauses, but a much slower pace. We decided to take the second choice, for the delay would be intolerable in a real-time procedure, and also because the information given at a frame changes relatively slowly, thus permitting to miss intermediate frames.

The final frame rate achieved was about three frames per second, for a full screen capture, and slightly higher for partial screen captures. The later case was the common, since only a small region in the screen displays the actual image.

4.4.2 Calibration procedure

The purpose of a calibration procedure is to find out the transformation to relate one coordinate system to another. Our objective is to track the contents of the ultrasound image into a coordinate system related to the patient. We recall from previous section the main equation which describes the system.

A pixel with coordinates $P_{\overline{\mathbf{x}}} = (x, y)$ in $\mathbf{U}$ will be transformed to some other coordinates $C_{\overline{\mathbf{x}}} = (x', y', z')$, and the equation linking them is:

$$C_{\overline{\mathbf{x}}} = P_{\overline{\mathbf{x}}} \cdot M_U^R \ \cdot M_R^T \ \cdot M_T^C \tag{4.2}$$

M_U^R and M_T^C are rigid transformations which depend on the set of parameters being calibrated. Table 4.2 presents the dependency for the phantoms evaluated in later sections. The translation and rotation operations are as defined in appendix A.

It is very important to achieve a proper estimation of the matrix M_U^R , since it determines the accuracy of the rest of the experiments. For instance, wrong values in M_U^R would convert B-frames acquired following a parallel raster into incoherent useless pattern. This becomes obvious after the volume image has been compounded: neighbouring regions do not seem to fit properly, depicting non continuous structures. However, similar problems occur no matter how well M_U^R has been computed, because

	Parameters	Z-shape	Surface	Point
	T_x	Y	Y	Y
M_U^R	T_y	Y	Y	Y
	T_z	Y	Y	Y
	T_x	Y	–	Y
	T_y	Y	–	Y
	T_z	Y	Y	Y
M_T^C	R_x	Y	Y	–
	R_y	Y	Y	–
	R_z	Y	–	–

Table 4.2: Identifiable parameters for each model to calibrate the transducer.

of the errors in the position provided by the tracking device. This effect will be shown in further sections.

A normal iteration starts with the grabbing of the image from the video output of the ultrasound device and the recording of the associated position of the sensor. Then, since the other transformations are fixed and known, the image can be transformed and processed using its 3–D position.

We have devoted some time in studying this matter. Relevant issues are divided into two categories: those concerning the numerical aspect of the estimation, and those which are specific to the ecography device. For the first introductory part, we devised a number of experiments that did not need the ecographer. That was necessary because, much of the time, the ecographer not being available to us, first we had to solve all the related numerical issues. After this initial part had been addressed, we were able to start more complex experiments, this time with the ecographer.

When we started working with the mini-bird tracking, it was necessary to spend some time understanding its functioning and the communication procedure to the PC via the serial port. For instance, we initially discovered simply by following a ruler with the receiver, that the matrix describing the position and orientation had a format different to that documented in the manual.

Next goal was to do some sort of calibration without the ecographer. Our aim was to set up properly all the elements (optimisation algorithms, models and numerical issues) with other experiments, calibrating, for instance, a stylus attached to the receiver. For this section, we reviewed a large bibliography in the field of robot calibration. The results of these experiments have been moved to appendix H, for the sake of readability.

A look at equation (4.2) reveals that there are two unknowns: M_U^R , which we want to find, and $C_{\overline{\mathbf{x}}}$, the final coordinates. Should we know the final position of a given pixel in the image, we could use this information to solve the equation. The basic idea is to build a phantom with special geometric properties so that we are able to know the position of the features appearing in the image. This is done by a proper setting of the final transformation M_T^C .

A possible configuration could be to use a single point as the reference landmark. This point would be set to be the origin in **C**, and for every slice imaging it we know
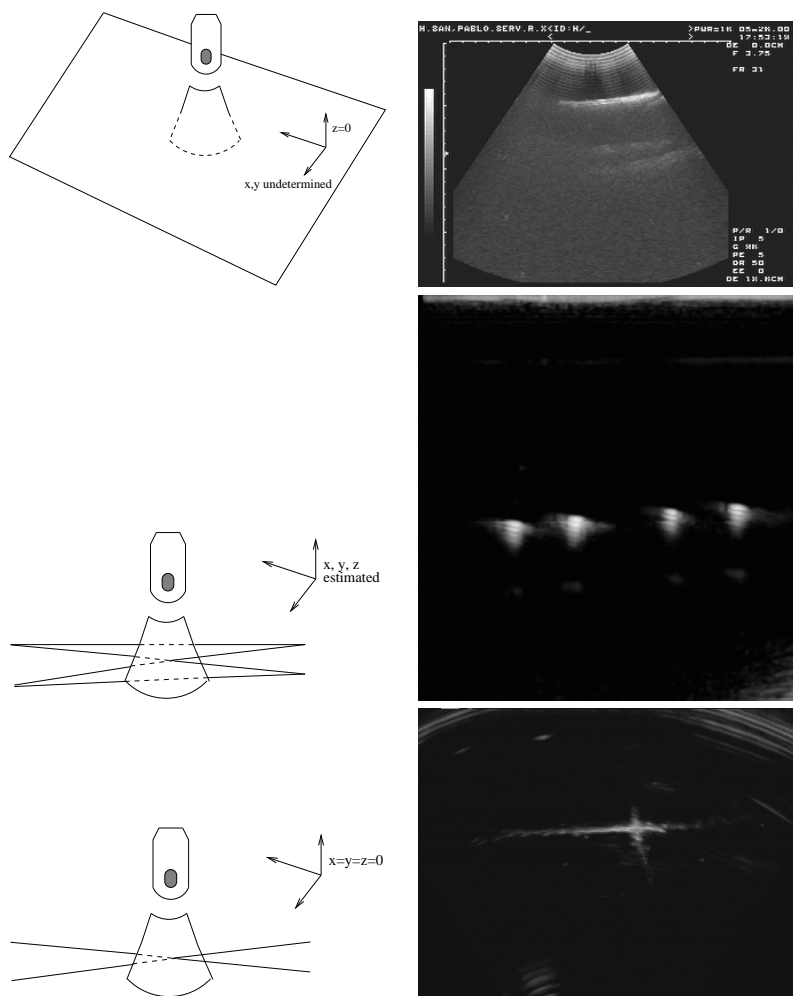
Figure 4.6: Models to estimate M_U^R

equation 4.2 is true for the coordinates of the pixels depicting it.

This idea has been successfully applied for the calibration of many devices. Rohling [79] describes several different architectures: a single point, two wires crossing perpendicular, a flat surface and a specially build device. Of these, the last is the one with best features: in addition to a low error, it permits the automatic segmentation of the landmarks therefore achieving a fully automatic calibration.

The mathematical methods required for parameter estimation do not depend on the choice of the model, i.e., the actual phantom employed. For the purpose of parameter estimation we have chosen the well-known Levenberg-Marquardt method. Appendix G provides a description of this method, together with some numerical

considerations. Although indeed the method we use is not a novelty, clear information regarding this application was difficult to find and had to be gathered from multiple sources, so for completeness we decided to include it in this thesis. Two issues included in the appendix are specially relevant to assess and improve the numerical results: the scaling of the parameters, and the condition number of result matrix.

We did not program the implementation the Levenberg-Marquardt method. With the aim of not dealing with all mathematical details, we used the libraries from Mathematica 4.0, Wolfram Research, Inc. [116]. This choice had the great advantage that most statistical and graphical functions were already implemented, but on the other hand it did not permit any modification of the algorithm itself. This would have been useful, for instance, to adapt the algorithm to work with several equations per iterations, instead of the standard single equation: equation 4.2 has actually three components, which must be combined into a single error variable.

We have experimented with three different phantoms for calibration. The first one, based upon a similar shape employed in stereotactic surgery to calibrate the CT slices, is used for this purpose for the first time. The second phantom we chose was the flat bottom of the calibration recipient. In order to fasten the process, we implemented an algorithm to automatically detect the line at the image produced by the surface. Unfortunately , numerical results showed to be unreliable, so, after the advices of some colleagues, we employed another, well known, phantom. This third phantom consisted on the point made by the crossing of two wires.

Each of the following three sections is devoted to the phantoms listed above.

4.4.3   Calibration using a Z-shape phantom

We investigated an alternative phantom inspired in a similar calibration problem which occurs in stereotactic surgery. In that procedure, it is necessary to estimate the position of some markers appearing in a CT image in an external coordinate system. The x and y coordinates are easy to compute given the pixel size, but in order to estimate the z a more complex computation is needed. The z can be estimated after the equations driving the particular geometry of the markers: the relative distance between the markers permits to position the CT scan.

This approach has the advantage that the x, y and z position of the landmarks appearing in the image can be estimated, thus providing much more information for each slice, and reducing the uncertainties in the equations.

See figure 4.7 for the scheme of all elements in the system. Note that the experiments in this sections have used the Optotrack as the tracking device. In order to let the tracker keep sight of the probe while excising all the degrees of freedom needed by the calibration, a set of IREDs had to be attached following a cylindrical fashion. Also, a pin-hole marker was attached to each end of the wires, so that their position relative to the tracker could be set.

Building the prototype, which was one of my responsibilities, was not an easy task because it demands a very high accuracy on the position of the anchors. As well, special pin-hole markers had to be constructed in the hospital workshop.

The IREDs in the reference object are continuously tracked in the Optotrack, and therefore so is the transducer. The calibration phantom consists on a box filled with isotonic water with four nylon wires (diameter=$0.18mm$). The procedure consists on imaging the wires with the ultrasound device, and the result is a set of slices similar to the one shown on the right hand side in figure 4.7. We remark that the diameter depicted is considerably bigger than the actual, thus making segmentation prone to error.

We have developed the equations to model the Z-shape phantom. We have included in figure 4.9 the constants and variables; despite the large number of labels, in short we simply want to estimate the out-of-plane coordinate z of the points $P_1 \cdots P_4$ as a function of their relative distances.

This geometric set may be regarded according to several models, depending on the information we use. For instance, one may only use the constraint that the first point on the left belongs to a line which leads to the equations $x = z = 0$. We have considered three different models. See figure 4.9 in page 151 for the meaning of the variables.

1. The wire I_1 has coordinates $\tilde{P}_1 = (0, 0, \chi)$ in **C**. χ is not known, so we only use the first two coordinates.

2. I_1 and I_4 have coordinates $\tilde{P}_1 = (0, 0, \chi)$ and $\tilde{P}_2 = (A, 0, \chi)$.

3. The 3–D coordinates of $\tilde{P}_{1...4}$ is a function of relative distances of the wires in the images. The following set of relationships can be deduced (equations hold

for i=0,1):

$$h_i = \frac{H\,l_i}{l_i + r_i} \tag{4.3}$$

$$w_i = \frac{W\,h_i}{l_i + r_i} \tag{4.4}$$

$$s_i = \sqrt{l_i^2 - w_i^2} \tag{4.5}$$

And the estimated coordinates of P_i in the coordinate system **C** are:

$$\tilde{P}_2 = (w_0, 0, h_0) \tag{4.6}$$

$$\tilde{P}_3 = (w_1, 0, h_1) \tag{4.7}$$

$$s_0 > s_1 \quad : \quad \begin{cases} \tilde{P}_1 = (0, 0, h_0 + s_0) \\ \tilde{P}_4 = (W, 0, h_1 + s_1) \end{cases} \tag{4.8}$$

$$s_0 < s_1 \quad : \quad \begin{cases} \tilde{P}_1 = (0, 0, h_0 - s_0) \\ \tilde{P}_4 = (W, 0, h_1 - s_1) \end{cases} \tag{4.9}$$

Equation (4.7) gives the coordinates of the two middle wires. The z-coordinates of P_1 and P_4 depend on whether the ultrasound slice is right-wise (as in the scheme) or left-wise. For brevity we have omitted the case when the slice is above the middle point.

Each setting actually includes all the information the previous had. While models 1 and 2 consider only 2–D information (the distance between the two vertical wires and the fact that they are coplanar), the third also estimates the third coordinate and it may show errors which were not taken into account for the others.

We have chosen to take the scaling parameters directly from the setting of the device and not to optimise them in order to shorten the number of variables in the resulting system of equations.

The final procedure is:

1. Locate the four ends of the wire to compute M_T^C .

2. Scan the wires, recording M_R^T at every acquisition. Make sure to exercise all degrees of freedom, and also take care not to pass the mid-point of the phantom (otherwise, the coordinates of the points P_2 and P_3 will have to be swapped for method 3).

3. Segment the four wires P_i in each slice, and estimate the coordinates $\tilde{P}_i$. This is currently done semi-automatically.

4. Run the optimisation method on the data.

Results of calibration using a Z-shape phantom

Table 4.8 lists the mean error for the methods described above. To double-check these results, we have computed the error not only for the model determining the
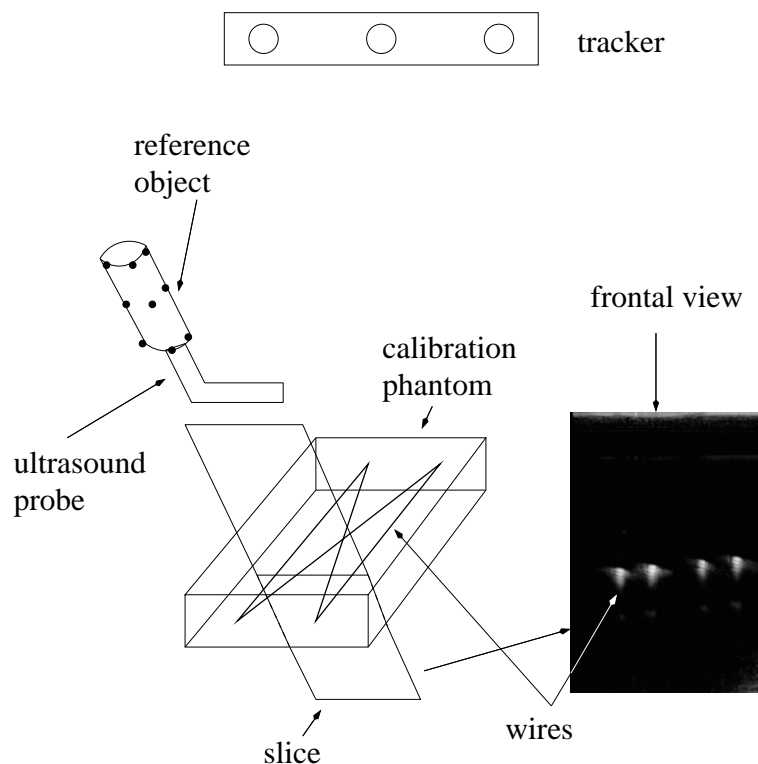
Figure 4.7: System for calibration with an Optotrack

optimisation, but also for the other models. This procedure has the advantage to show errors that the model may have been unable to determine. For instance, model 1 and 2 do not estimate the error in z which, when computed using the model 3, happens to be quite large. Similarly, error for model 1 seems to be very low, 0.6 and 0.2, but these numbers increased when other, more complete models were used.

Model 3 had initially very poor results: it converged to a solution with double RMS error than the others. We suspected that the minimum had been shadowed and the method had got trapped into a local solution. To solve this, we used solution from method 2 to discard the slices with an error higher than $10\,mm$. This is justified because these outlayers do not contribute to a solution with similar error to the other two, and they may be produced by tracker synchronisation errors. After the discard, we obtained a solution with a bounded known 3–D error, which was the one we used in our experiments. This has been labelled as method 4 in the results table 4.8.

Despite all the efforts, the error in the z coordinate was for all models much larger that for x and y. We have investigated the causes of the error in the third coordinate, and we have found it to be overestimated. Let's have a look at the equations of the model, this time considering noise in the position. Equation 4.3 becomes:

$$\tilde{h} = \frac{(\tilde{H} + \varepsilon)(\tilde{l} + \epsilon)}{(\tilde{l} + \epsilon) + (\tilde{r} + \epsilon)} \approx \frac{H\,l}{l + r} + \frac{H}{l + r}\epsilon + \frac{l}{l + r}\varepsilon \approx h + \frac{H}{l + r}\epsilon \approx h + 10\epsilon \quad (4.10)$$

where ε is the error in measuring the distance between the anchors of wires and ϵ is the error when measuring the distance between the segmented points.

The more relevant error is ϵ because it is magnified by the quotient $H/(l + r) \approx$ 10. To evaluate ϵ we measured the real diameter of the nylon wire $(0.18\,mm)$ and compared it to one apparent in the image $(0.7\,mm)$. Therefore, $\epsilon = 0.5\,mm$ and the error magnitude is around $5\,mm$.

This magnification error was very inconvenient, there was no way to improve the results. Although we employed the calibrations for the initial experiments in section 4.5.1, when we changed to the Minibird to track the position we decided that this phantom was too demanding in accuracy for any misalignment in the wires caused errors. Also, one requirement was to read the final position of the wires with the stylus, which could not be done with a single magnetic device. Therefore, we investigated the performance of other phantoms.

		Comparative method							
		1 RMS (Std)		2 RMS (Std)		3 RMS (Std)			Samples
		x	y	x	y	x	y	z	
Optimisation method	1	0,6 (0,2)	0,2 (0,6)	1,1 (0,6)	3,1 (2,2)	1,0 (0,5)	2,1 (2,0)	3,6 (5,3)	1084
	2	0,6 (0,2)	0,3 (0,8)	0,7 (0,2)	0,3 (0,9)	0,6 (0,2)	0,3 (0,9)	3,2 (4,7)	1092
	3	2,3 (2,3)	1,2 (6,7)	3,3 (5,4)	8,1 (4,1)	2,2 (2,8)	5,3 (4,7)	6,2 (4,1)	1112
	4	1,5 (0,7)	0,7 (1,1)	2,1 (0,9)	0,6 (1,0)	1,6 (1,0)	0,5 (1,0)	3,1 (3,9)	1112

Figure 4.8: Calibration errors for the different methods. Each row shows the errors with its standard deviation for each dimension. The error has been computed in the three schemes as described in the text.
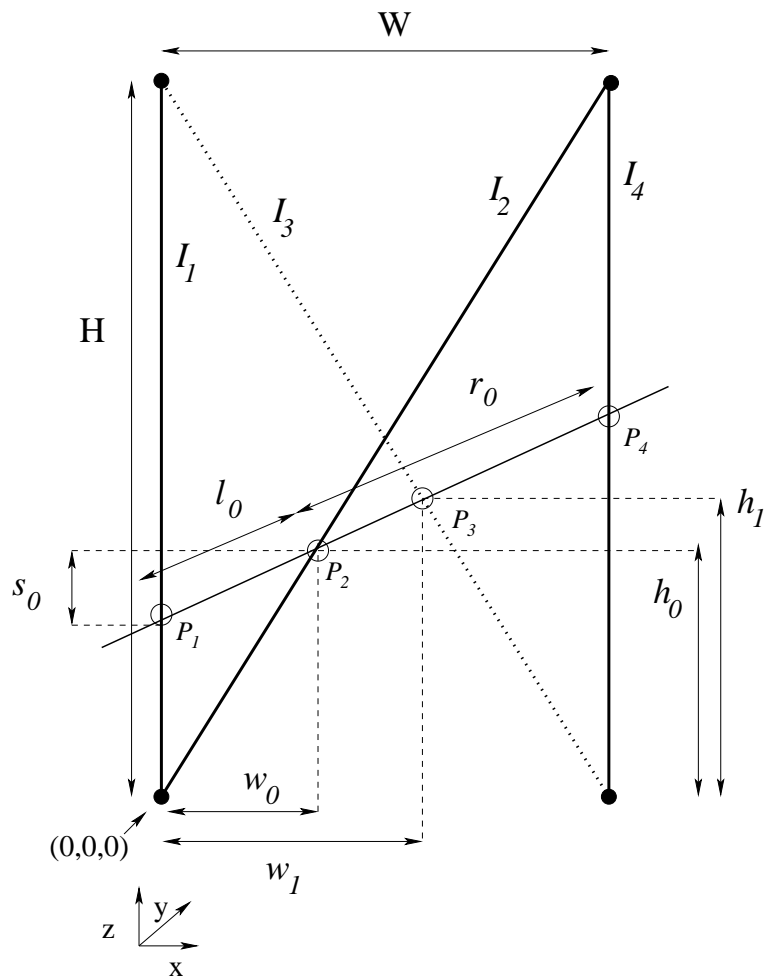
Figure 4.9: Scheme of the phantom to calibrate the ultrasound images. The four wires (numbered $I_1 \cdots I_4$ consecutively from left to right) end in the points marked as black circles and their intersection to the ultrasound scan is marked with white circles (numbered $P_1 \cdots P_4$). The three wires drawn in dark form a figure whose features are explained in the text. The opposite triangle would have similar features and naming, which have been omitted in the picture for clarity.

4.4.4   Calibration by means of a flat surface

The bottom of the calibration bucket appears neatly as a single line when imaging an object, so it is an obvious candidate to become a calibration phantom. Some convenient properties are:

- it does not require special or accurate designs.

- the ecographer operator can locate and image it very easily (small phantoms can be very difficult to track).

- the signal has a distinct and regular shape in the image, thus making feasible an automatic detection algorithm.

The group from Cambridge has actually built and patented a phantom with characteristics similar to a flat surface and improved reflectance and homogeneity. In effect, in order to obtain a well posed data set, it is required to exercise all the degrees of freedom when imaging the device, but the ecography presents false signals when the transducer is not perpendicular to the surface. See, for instance, images in figure 4.12.

Despite the disturbing artifacts, the mentioned properties were still very convenient, so we decided to further investigate the calibration with this phantom. With this goal we followed the following steps:

1. we adhered an ecography-opaque linen to the bottom surface, making sure to keep it as flat as possible and take air bubbles away.

2. we scanned the surface, trying to exercise all degrees of freedom. We grabbed the video image in live.

3. we segmented manually the surface, depicted as a line, in each frame.

4. we run the optimisation algorithm after setting it to model a plane.

The third step soon became very tiresome, because it was repetitive and very lengthy. Therefore, we decided to spend some time designing an automatic detection algorithm. This algorithm was not designed to process the frames in real time, but rather to be robust and accurate.

The idea is to detect the line as the highest valued row of the y-derived image. This value is computed at a range of rotations, and the highest of them is chosen. Figure 4.10 give the details in pseudo-code:

① rotate the image with a trial angle α

② compute the derivative in the y axis using finite differences.

③ for each row in the image, add the value of all its pixels.

④ store the higher value in the row image; keep the angle α and the position y.

⑤ repeat for the range of angles.

⑥ take the highest value.

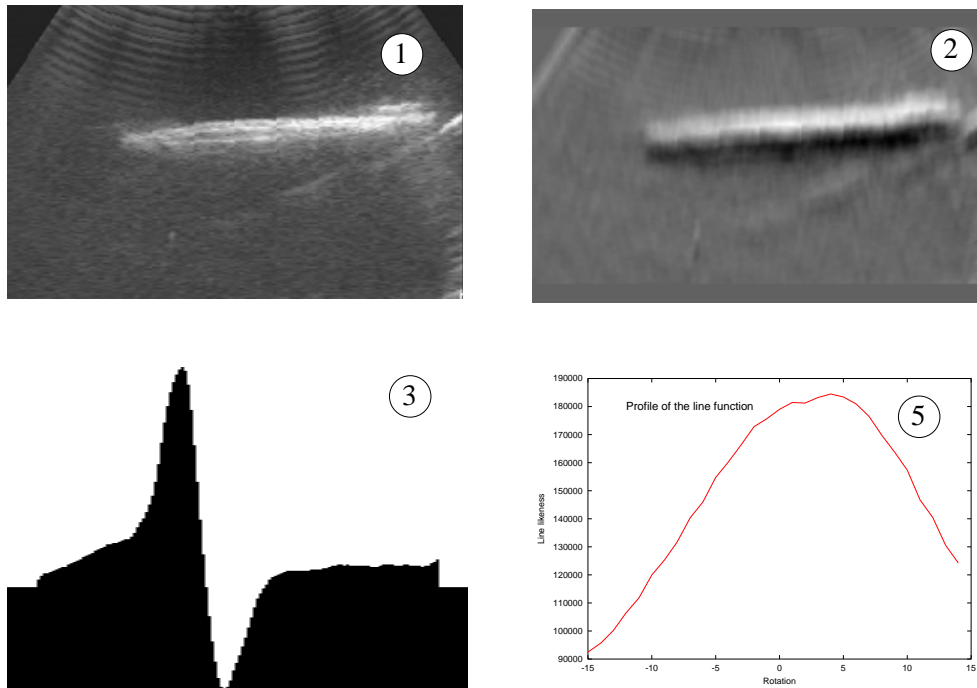**Figure 4.10:** Pseudo-code of the algorithm to detect the surface line.

Figure 4.11: Algorithm to automatically detect the line made by the flat surface in the ecography. From top to bottom, left to right: a) original image b) y derived image ② c) profile of ③ d) profile of ⑤ (numbers refer to figure 4.10)
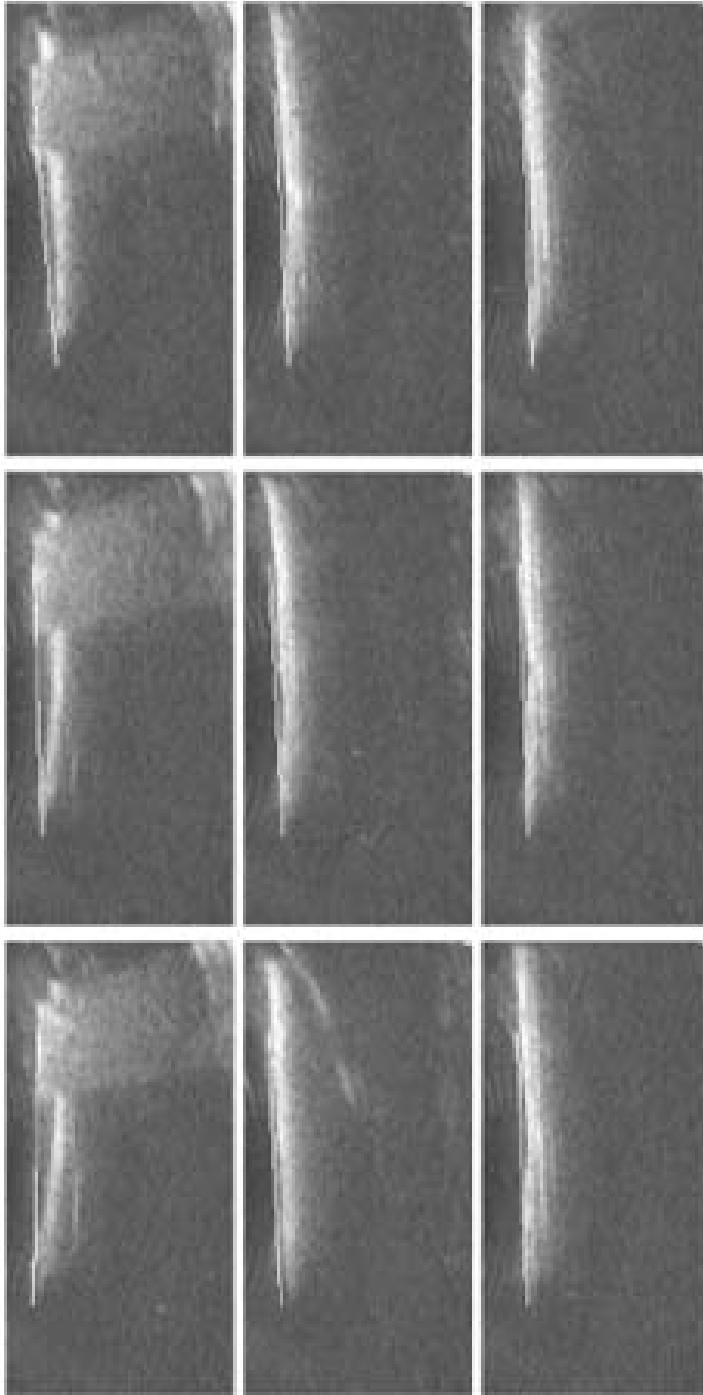
Figure 4.12: Automatic detection of bottom line in ecographies. Although the algorithm works well for all cases, in the three top frames the result is disturbed by artifact signal of the surface.

Despite all our efforts, the experiments showed this method of calibration not to be accurate enough. We acquired four series of data with the same settings, this is to say, without moving the phantom or the Minibird, and run the calibration algorithm described above. Results in tables 4.3 and 4.4 are very disappointing because, although the accuracy (RMS error) is reasonable, the numerical values of the solution vary a lot, while they are expected to be the same. Results were also very unstable when we made a number of new sets by combining random samples of the previous.

S.	M_T^C			M_U^R								
	T_z	R_x	R_y	T_x	T_y	T_z	R_x	R_y	R_z	S_x	S_y
	(mm)	(deg)			(mm)			(deg)			
1	57.84	2.59	8.05	-42.3	100.11	-26.61	178.58	-15.63	28.26	0.013	0.45
2	30.82	-5.14	2.05	2.44	4.73	-13.55	87.54	-106.33	-151.46	0.02	0.22
3	32.9	-1.26	3.11	-35.48	74.39	-34.15	-179.93	-173.89	87.86	0.22	0.34
4	48.45	-1.87	3.4	-64.04	-40.51	-50.97	26.73	49.21	-17.44	0.040	0.97

Table 4.3: Numerical values of calibration by means of a flat surface

S.	#	RMS.	StdDev	C.N.
		(mm)	(mm)	
1	772	3.1	3.94	417
2	768	3.64	4.69	1835
3	698	2.61	3.39	143
4	482	2.12	2.77	1751

Table 4.4: Numerical results of calibration by means of a flat surface. Despite the accuracy, values show little repeatability.

There can be a number causes of the bad posing of the data: the artifacts, which produce error in the location of some frames, the tracking errors, higher with non static acquisitions, and also perhaps that the model is too loose to permit a proper convergence when the input data is noisy.

Because the previous error sources were intrinsic of the model and seemed hard to improve, we finally rejected this method and decided to use the well-known cross wire. We would like to point out that the decision was taken under the pressure of time at the second stage in London, and also after the advice of the colleagues in the laboratory who had already achieved some proper results with their own system.

4.4.5 Calibration using cross-wires.

During the second stage in London, my research could not go any further because the calibration step, up to that time, had not been successful. Therefore it was crucial to design a safe and robust algorithm, which we did with the advice of Dr. Graeme P. Penney, who I thank. We decided to employ the well known crossing wires method,
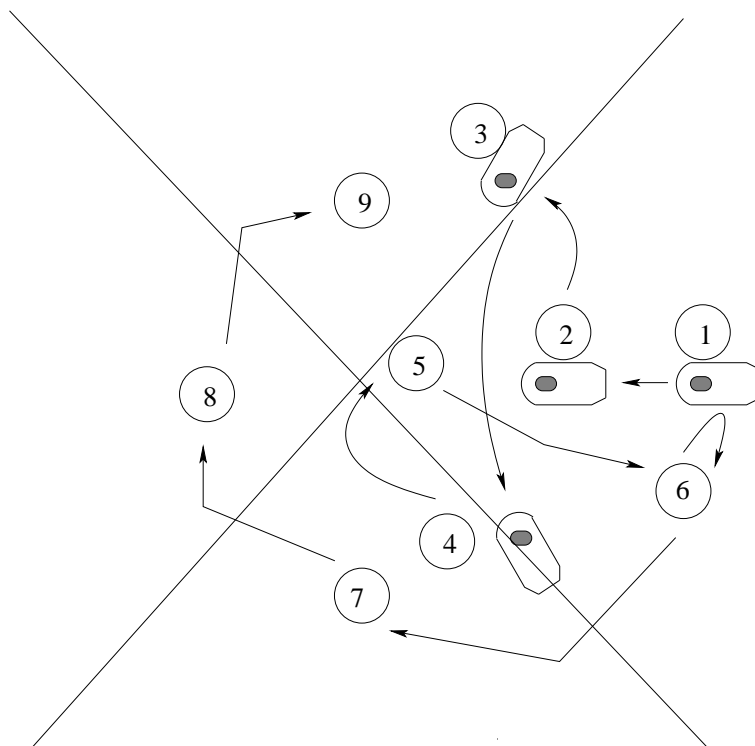
Figure 4.13: It is important to exercise all degrees of freedom when scanning the calibration phantom. See text for details.

and to hold the transducer each time a frame had to be captured instead of live video framing. This approach permits to focus properly the field of view to include the point to be imaged, and presumably would reduce the error in positioning the tracker produced by the movement in the previous experiments.

After doing the first trial, to our deception, the method failed at all to converge. We examined the data, and found that for a number of frames the tracker had given a completely wrong position. The failure was due to the nature of the magnetic field employed by the device, and was easy to detect because the sign of the angles of the orientation had swapped. This would occur some times when the receiver crossed the z-plane of the tracker; even though this effect is reported in the specifications manual and we had taken it into account when designing the software, in a number of cases our software interface failed to detect the error and produced the outlayers.

We took two approaches to minimise this effect; first, we tilted the emitter box with respect to the plane where the phantom was placed until the whole process could be done without crossing the $z = 0$ plane. Also, and because the previous did not seem to eliminate entirely the effect , we discarded manually those data which had obvious wrong orientation.

Another important issue was, again, to make sure that all the degrees of freedom

Probe	Scale	M_T^C			M_U^R							
		T_x	T_y	T_z	T_x	T_y	T_z	R_x	R_y	R_z	S_x	S_y
(MHz)		(mm)	(mm)	(mm)	(mm)	(mm)	(mm)	(deg)	(deg)	(deg)		
10	N	-304.83	15.18	-75.16	86.19	12.58	-11.77	-2.07	22.24	-83.95	0.0938	0.0938
	Y	-304.91	15.27	-75.21	86.99	11.26	-12.74	0.411	22.27	-79.08	0.098	0.0886
3.5	N	-266.11	15.04	-67.26	84.09	58.99	-35.35	-2.61	-20.19	-87.68	0.233	0.233
	Y	-266.01	15.32	-67.23	84.43	56.2	-30.5	-3.5	-16.95	-88.06	0.213	0.235
6.5	N	-349.52	29.67	-77.85	129.16	22.4	-3.44	-1.45	-6.79	-92.75	0.163	0.163
	Y	-349.41	29.86	-77.89	132.36	19.44	-1.61	-3.92	-6.42	-92.24	0.152	0.147

Figure 4.14: Numerical values of calibrating the probes. The column Scale is Y when scaling variable have been optimised, N when they have been estimated. M_T^C and M_U^R are not meant to be the same for calibration with different transducers.

Probe	Samples	Scale	RMS		StdDev	Condition
MHz			mm	pix.	mm	number
10	91	N	3.98	42	1.73	15.31
		Y	4.02	42	1.71	19.92
3.5	93	N	6.74	29	2.81	14.18
		Y	6.43	28	2.83	20.59
6.5	82	N	4.29	26	1.62	13.68
		Y	4.16	27	1.57	16.64

Figure 4.15: Accuracy of the calibration using a cross wire.

were exercised. To ensure this point, we designed a protocol to be followed when acquiring the data. This consisted of a sequence of movements and rotations to image the crossing point in all possible angles and distances.

Figure 4.13 shows the pattern of positions to scan the phantom:

- At several distances to the cross (1,2).

- Spinning round the cross to other angles in the same quadrant (3,4).

- Perpendicular over the cross (5).

- Turn 90 deg the transducer, although it may be difficult to get a good reading. (6).

- Turn again 90 deg the transducer and repeat 1-6

- Repeat for other quadrants.

- Also, for each position take more than one snapshot, each depicting the point in a different pixel position in the image.
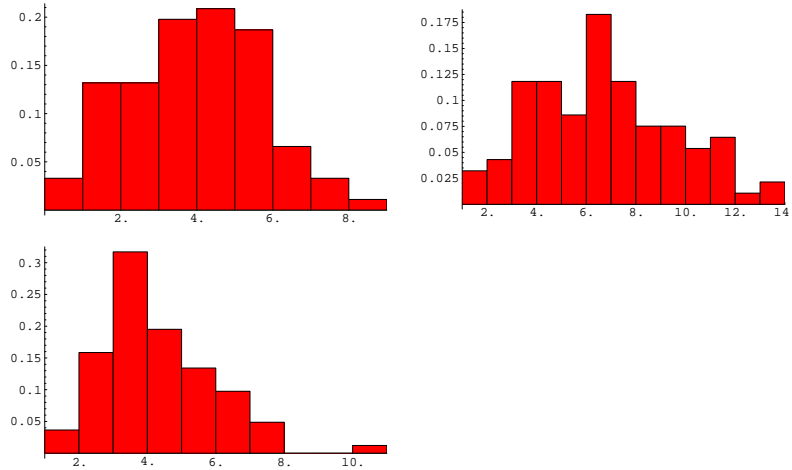
Figure 4.16: Histogram of the calibration errors for transducers 10 and 3.5 MHz (top) and 6.5 MHz (bottom). The sum of bars for each histogram is 1.

We performed the calibration experiments under the conditions stated above for the three transducers available in the device. They differ in the frequency employed to scan the issues; the highest it is, more detail can be captured, but the penetration is lower.

Numerical values of the registrations were consistent and reproducible; see table 4.14 for a samples of the output values. This table presents two sets of results for each transducer; the first, labelled as **N**, was obtained without including the scaling factors in the optimisation scheme. Instead, the numbers have been estimated with the rulers appearing in the ecography, which are result of a calibration process internal to the ecographer.

For the second row, labelled as **Y**, these factors were included, and it is included for comparison purposes since results in the following sections employ only the first set. The reason why not to optimise them is that the process tends to underestimate these numbers while attempting to shorten the distance between the points. For none of the optimisations we had any estimation of the position of the cross within the tracking coordinate system, but the data was well set and convergence was achieved anyway.

The accuracy is given in table 4.15. For each calibration, we give three statistical numbers: the root mean squared error, the standard deviation and the condition number. The rms is very large compared to those of published papers: 4 to 6 mm, which may be up to one forth of the image. While this was worrying, at this stage we could not do any further to reduce it, so we decided to continue with the experiments, and see if the composition of the frames would be problematic due to this error. On the other hand, the condition number was low so presumably the data was well-posed and the mathematical models properly chosen.